

Supporting Information for: “Role of hemibonding in the structure
and ultraviolet spectroscopy of the aqueous hydroxyl radical”

Bhaskar Rana and John M. Herbert*

November 10, 2020

*herbert@chemistry.ohio-state.edu

1 Stability of QM/MM Simulations

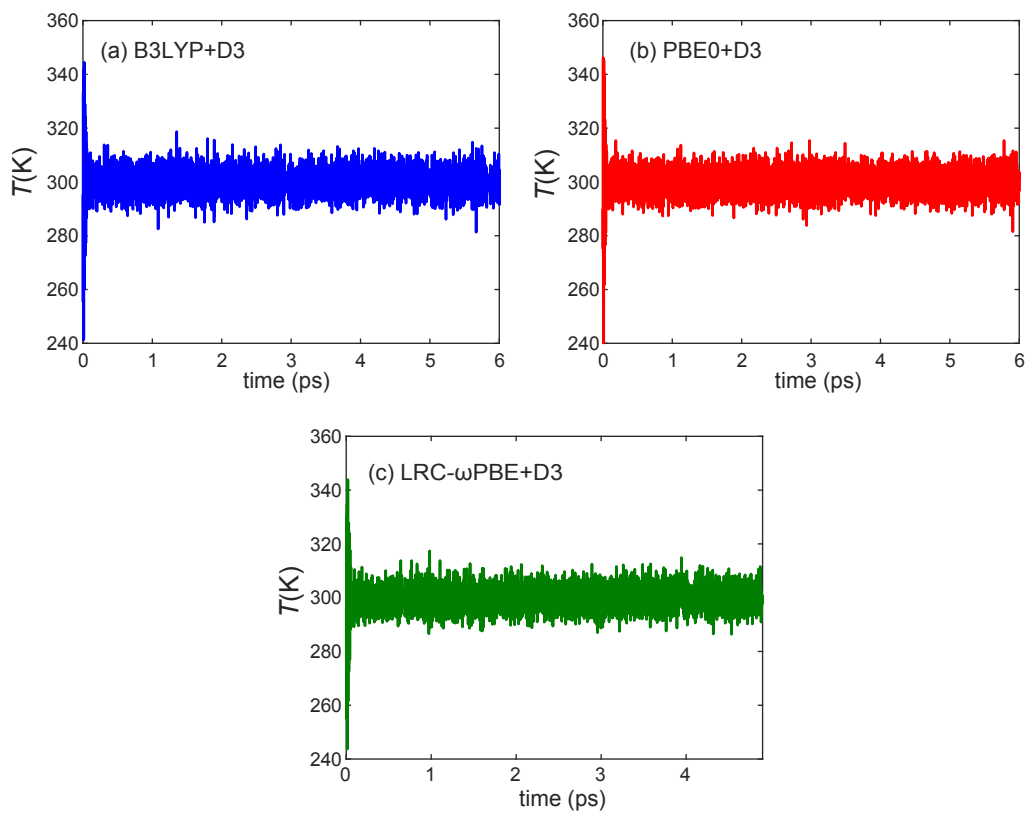


Figure S1: Time evolution of instantaneous temperature for QM/MM simulations performed using (a) B3LYP+D3, (b) PBE0+D3, and (c) LRC- ω PBE+D3. The NVT trajectories (using a Nosé-Hoover thermostat) were initiated from an equilibrated liquid water trajectory; fluctuations settle within 500 fs, which was discarded as the equilibration time. Average temperatures are $\langle T \rangle = 300.0 \pm 4.9$ K (B3LYP), 300.0 ± 4.9 K (PBE0), and 300.0 ± 5.0 K (LRC- ω PBE).

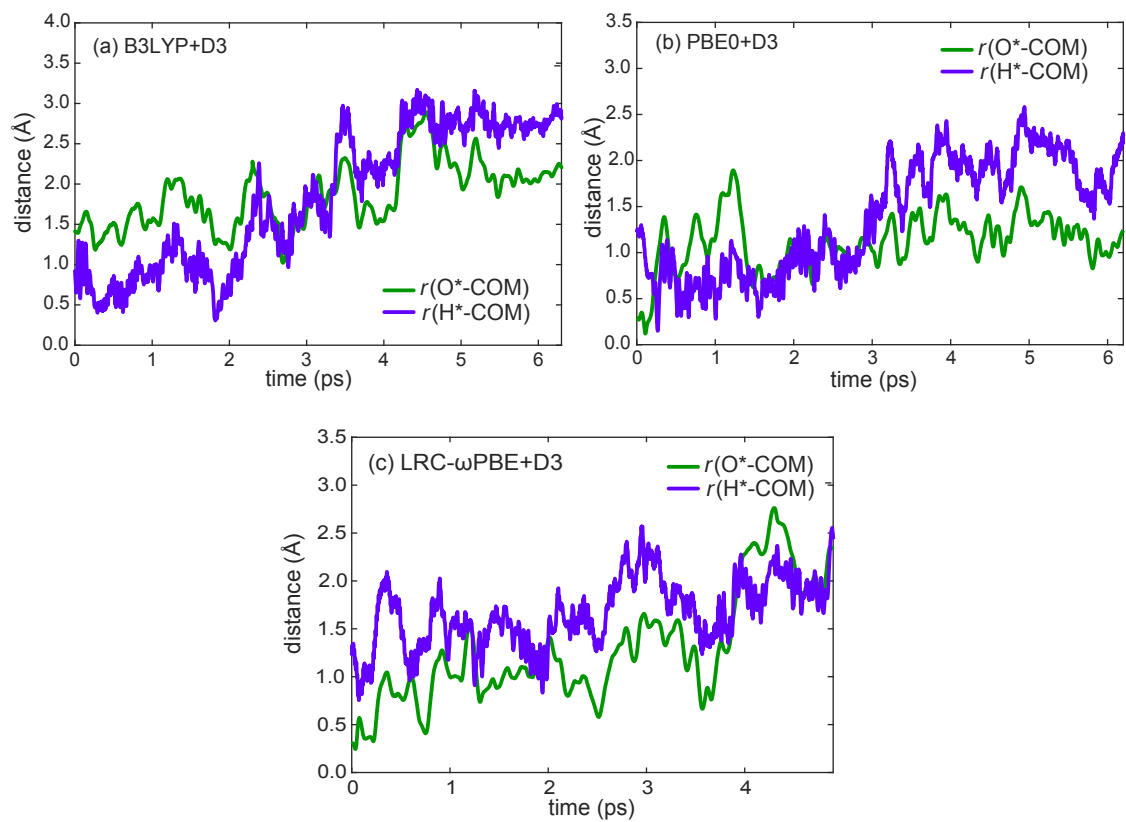


Figure S2: Time evolution of the distance between the O* and H* atom and the QM center of mass, during simulations with (a) B3LYP+D3, (b) PBE0+D3, and (c) LRC- ω PBE+D3.

2 Radial Distribution Functions

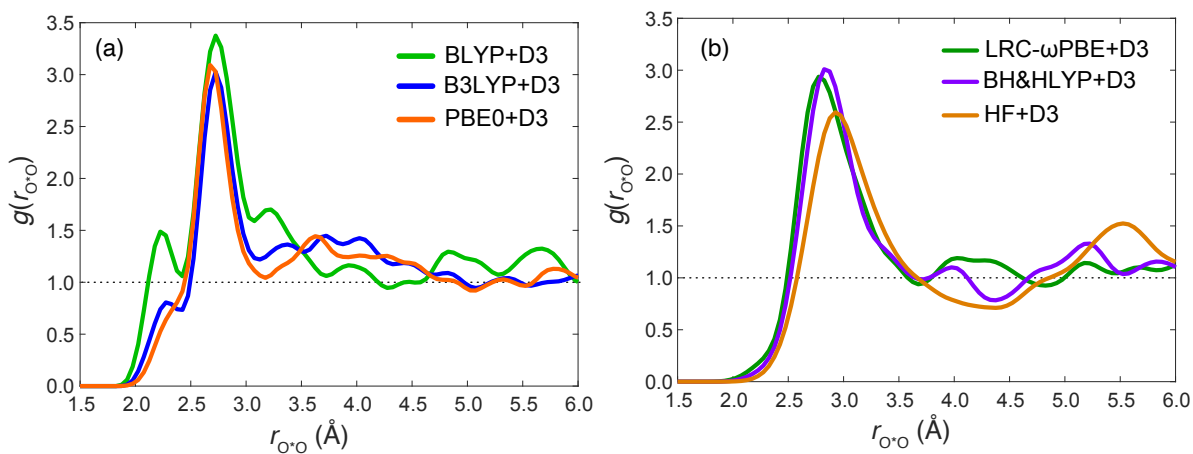


Figure S3: Comparison of RDFs $g(r_{O^*O})$ for the $O^* \cdots O$ distance in $^{\bullet}\text{OH}(\text{aq})$, where O^* indicates the hydroxyl oxygen. Results were obtained from QM/MM simulations using various density functionals, as indicated. They are separated here into (a) functionals with $\leq 25\%$ exact exchange, each of which predicts a feature (or at least a shoulder) at $r_{O^*O} \approx 2.3 \text{ \AA}$, indicative of hemibonding; versus (b) functionals with larger amounts of exact exchange, for which no such feature is observed. The B3LYP+D3, PBE0+D3, and LRC- ω PBE+D3 results shown here are the same as the ones shown in Fig. 2.

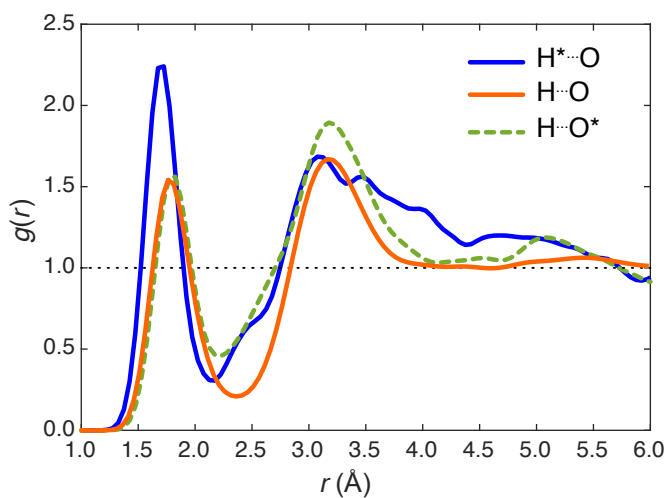


Figure S4: Comparison of various $O \cdots H$ RDFs obtained from QM/MM simulations using PBE0+D3. Atoms O^* and H^* belong to the $^{\bullet}\text{OH}$ radical, whereas O and H refer to water. Covalent bonds have been excluded from the averaging so that $g(r_{OH})$ represents the RDF for hydrogen bonds only. The corresponding data for B3LYP+D3 and LRC- ω PBE+D3 are shown in Fig. 3.

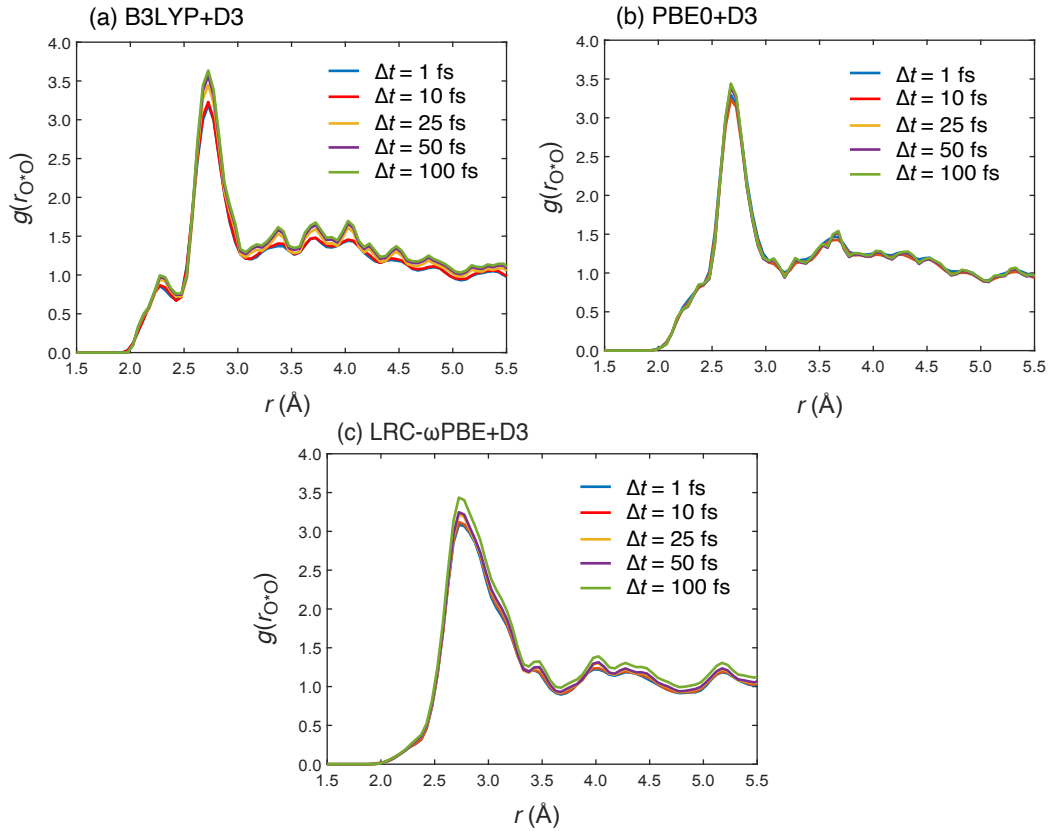


Figure S5: Comparison of $g(r_{O^*O})$ computed with different set of the snapshots, where the data points are separated in time by various intervals Δt , for trajectories obtained using (a) B3LYP+D3, (b) PBE0+D3, and (c) LRC- ω PBE+D3. The plots for $\Delta t = 1$ fs use all of the data and are the same ones shown in Fig. 2. Other values of Δt use only subsets of the data to compute $g(r_{O^*O})$, and this comparison demonstrates that the short-range liquid structure (up to the first local minimum) is converged with respect to sampling.

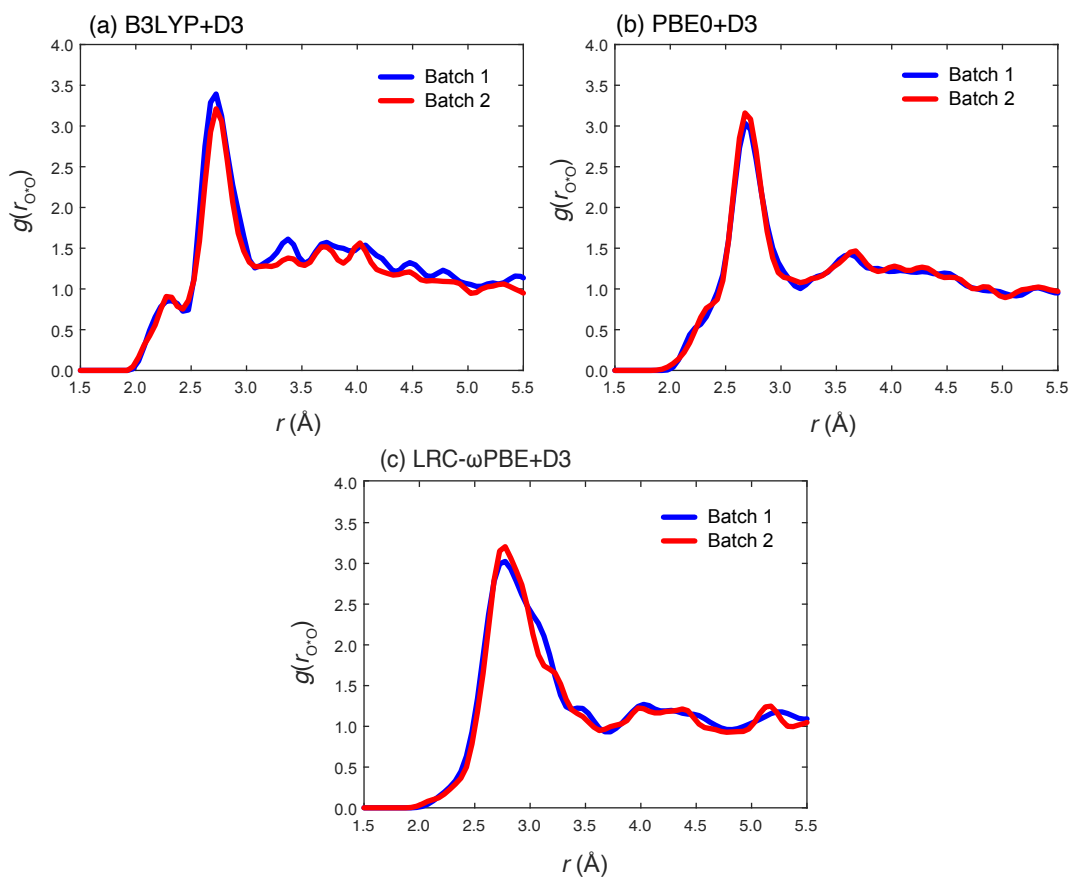


Figure S6: Comparison of $g(r_{\text{O-O}})$ computed with two different batches of snapshots, with data points separated by $\Delta t = 50$ fs. Batch 1 corresponds to the $\Delta t = 50$ fs data set used in Fig. S5, and the other data set consists of snapshots offset from those by 25 fs in time. As in Fig. S5, good agreement up to the first local minimum suggests that the short-range structure is converged.

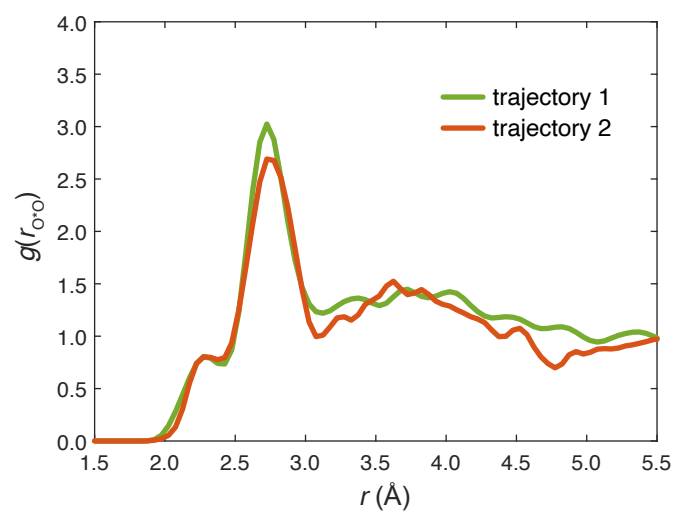


Figure S7: Comparison of $g(r_{O*O})$ computed from two independent B3LYP+D3 trajectories with different starting geometries.

3 Spin Densities

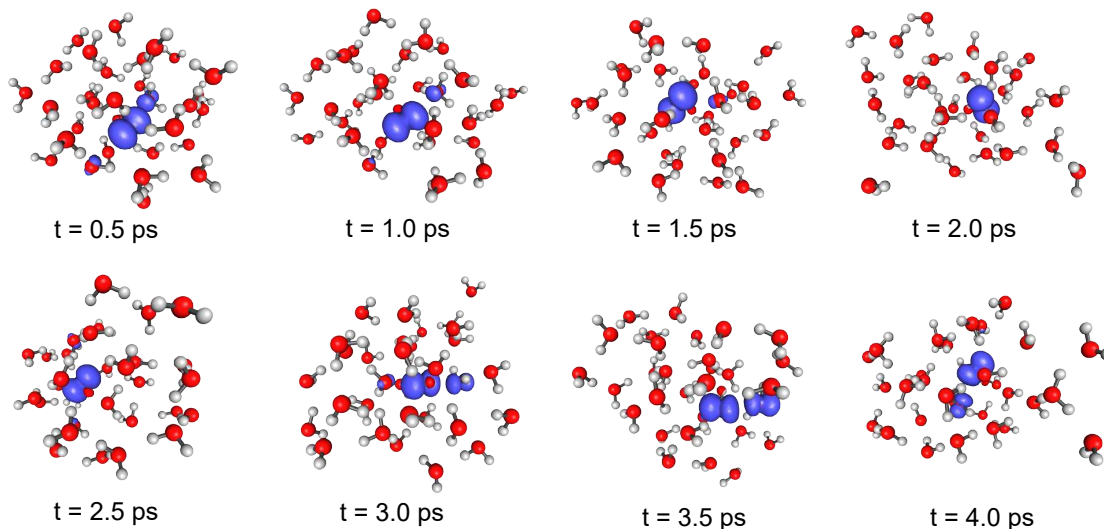


Figure S8: Time evolution of the spin density $\rho_\alpha(\mathbf{r}) - \rho_\beta(\mathbf{r})$ for the B3LYP+D3 trajectory, plotted using an isocontour value of 0.003 a.u.. (QM water molecules are shown.) In most snapshots, the spin density is delocalized over both the $\cdot\text{OH}$ moiety and a nearby water molecule, suggesting that hemibonded configurations are visited frequently.

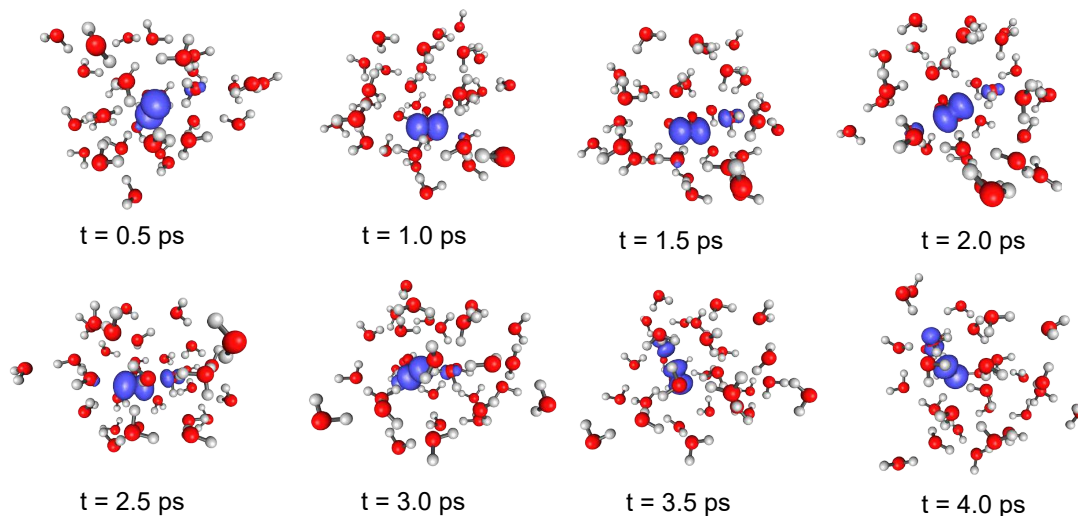


Figure S9: Time evolution of the spin density $\rho_\alpha(\mathbf{r}) - \rho_\beta(\mathbf{r})$ for the PBE0+D3 trajectory, plotted using an isocontour value of 0.003 a.u.. (QM water molecules are shown.) The behavior is similar to the B3LYP+D3 results and suggests a propensity for hemibonding.

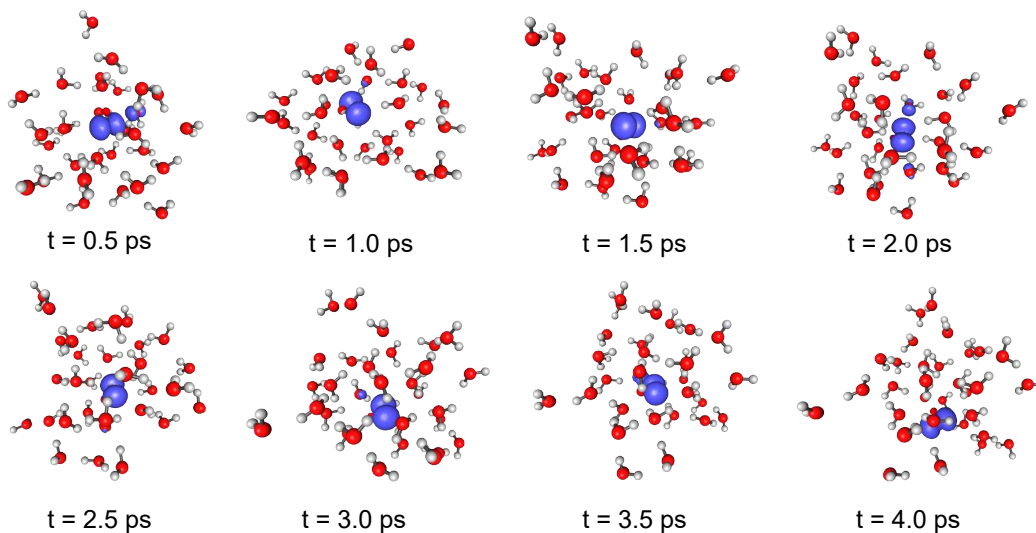


Figure S10: Time evolution of the spin density $\rho_\alpha(\mathbf{r}) - \rho_\beta(\mathbf{r})$ for the LRC- ω PBE+D3 trajectory, plotted using an isocontour value of 0.003 a.u.. (QM water molecules are shown.) The spin density is localized on the $\cdot\text{OH}$ moiety in most snapshots, suggesting that hemibonded configurations are visited infrequently.

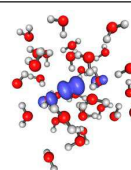
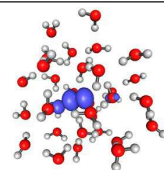
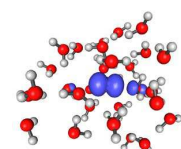
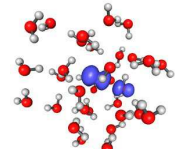
structure	sum of charges, q_{OH} (a.u.)	sum of spin charges, s_{OH} (a.u.)	SOMO (initial)	SOMO (relaxed)
A	-0.06 (before) -0.04 (after)	0.83 (before) 0.90 (after)		
B	-0.05 (before) -0.10 (after)	0.91 (before) 0.83 (after)		

Figure S11: Two snapshots extracted from the B3LYP+D3 trajectory and relaxed via several hundred QM/MM geometry optimization steps. Sums of the Mulliken charges on the hydroxyl moiety (q_{OH}) are shown, along with the corresponding sum of the Mulliken *spin* charges (s_{OH}), both before and after relaxation in either case. No significant changes are observed during the relaxation, in these and other snapshots. This suggests that when delocalized hemibonding is observed, the hemibonded configurations are inherent structures of $\cdot\text{OH}(\text{aq})$, rather than transition states or other transient fluctuations.

4 One-Dimensional Probability Distributions

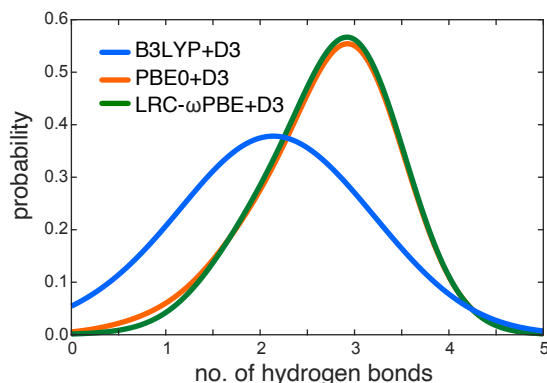


Figure S12: Distribution of the number of water-hydroxyl bonds for different trajectories. These are overlays of the distributions that are plotted separately in Fig. 4.

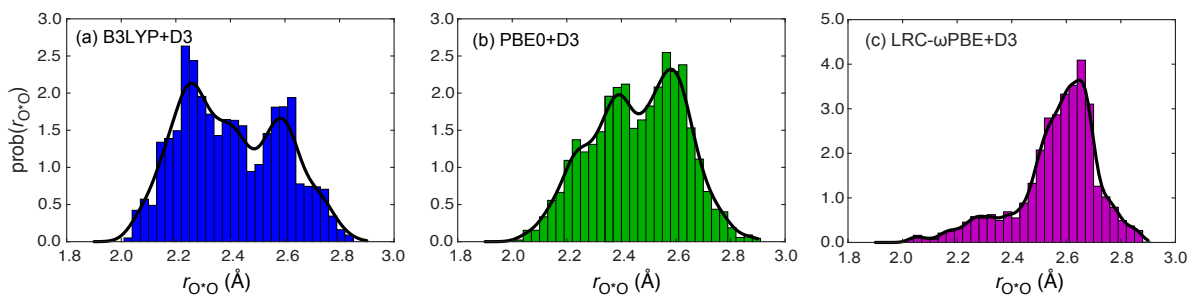


Figure S13: Probability distributions of r_{O^*O} for QM/MM simulations performed using (a) B3LYP+D3, (b) PBE0+D3, and (c) LRC- ω PBE+D3. Black curves represent fitted probability distributions.

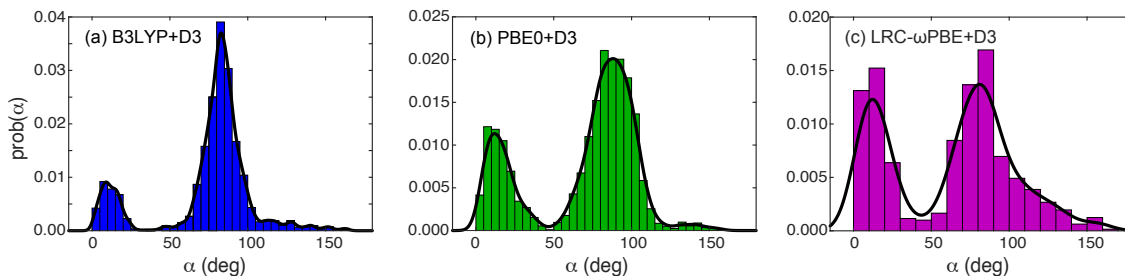


Figure S14: Probability distributions of the angle α (as defined in Fig. 1) for QM/MM simulations performed using (a) B3LYP+D3, (b) PBE0+D3, and (c) LRC- ω PBE+D3. Black curves represent fitted probability distributions.

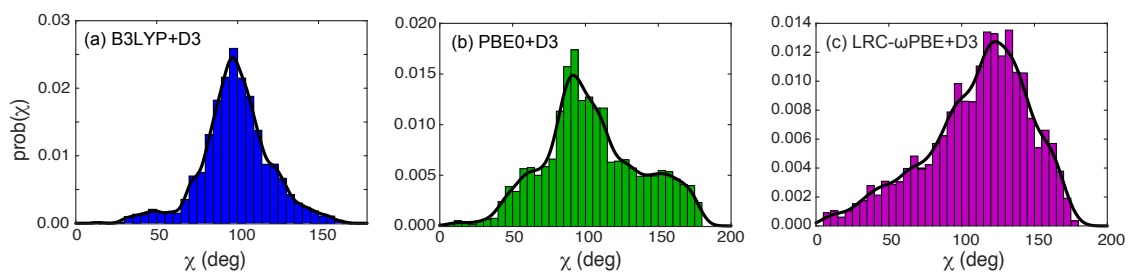


Figure S15: Probability distributions of the angle χ (as defined in Fig. 1) for QM/MM simulations performed using (a) B3LYP+D3, (b) PBE0+D3, and (c) LRC- ω PBE+D3. Red curves represent fitted probability distributions.

5 Two-Dimensional Joint Probability Distributions

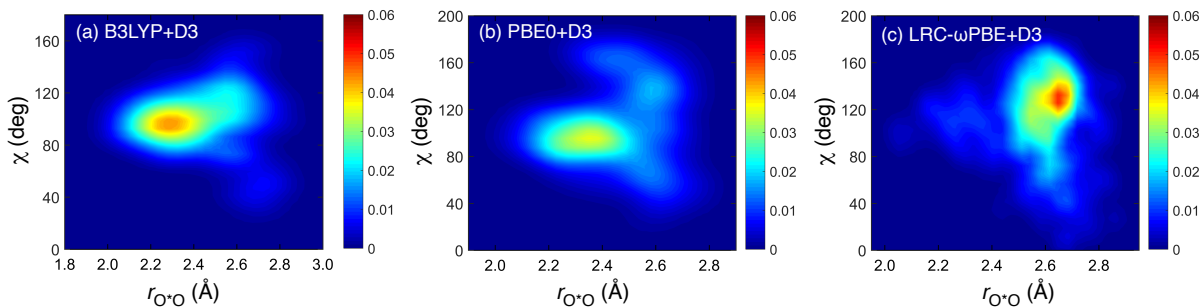


Figure S16: Joint probability distributions for r_{O^*O} and χ , from simulations using (a) B3LYP+D3, (b) PBE0+D3, and (c) LRC- ω PBE+D3. Definitions of the geometrical variables can be found in Fig. 1.

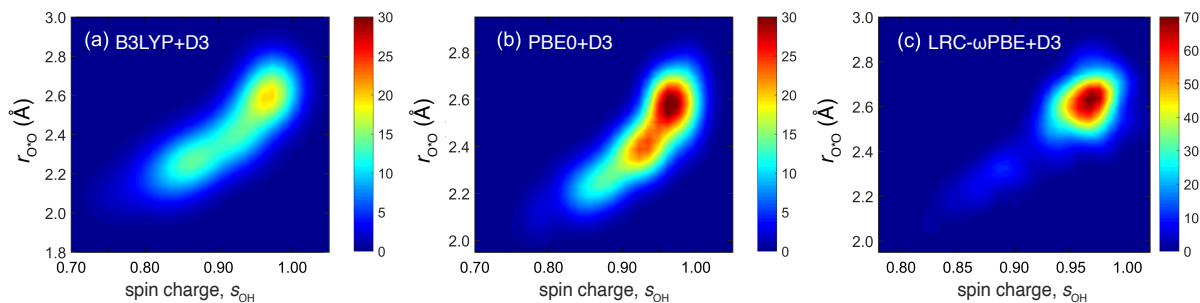


Figure S17: Joint probability distributions for r_{O^*O} and the spin charge on the radical (s_{OH}), obtained from simulations using (a) B3LYP+D3, (b) PBE0+D3, and (c) LRC- ω PBE+D3.

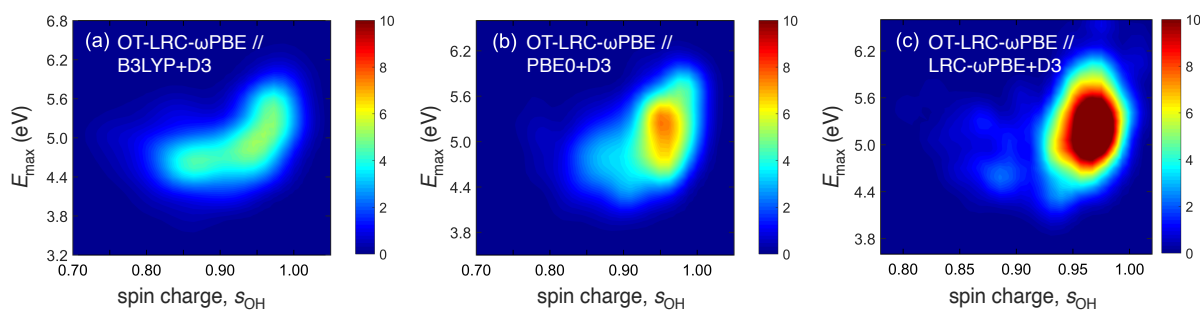


Figure S18: Spin charge on the hydroxyl moiety (s_{OH}) versus the estimated absorption maximum E_{max} , for QM/MM simulations performed using (a) B3LYP+D3, (b) PBE0+D3, and (c) LRC- ω PBE+D3. The absorption maximum is estimated using Eq. (6). Panel (a) of this figure is the same as Fig. 9.

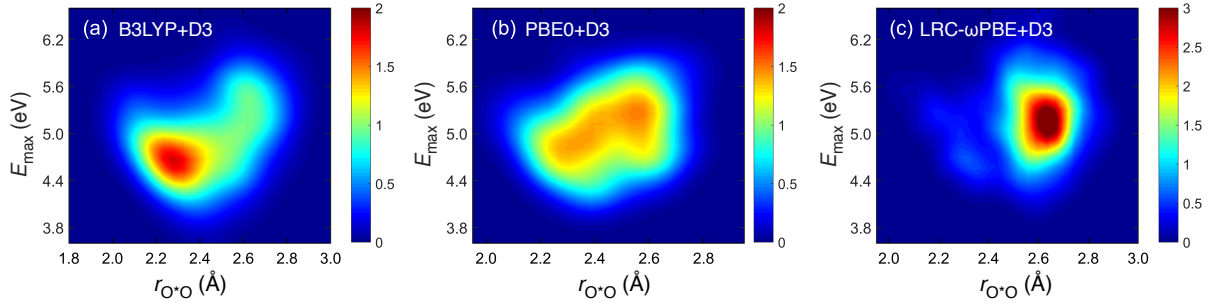


Figure S19: Distance r_{O^*O} versus the estimated absorption maximum E_{\max} , for QM/MM simulations performed using (a) B3LYP+D3, (b) PBE0+D3, and (c) LRC- ω PBE+D3. The absorption maximum is estimated using Eq. (6).

6 Tuning Plots

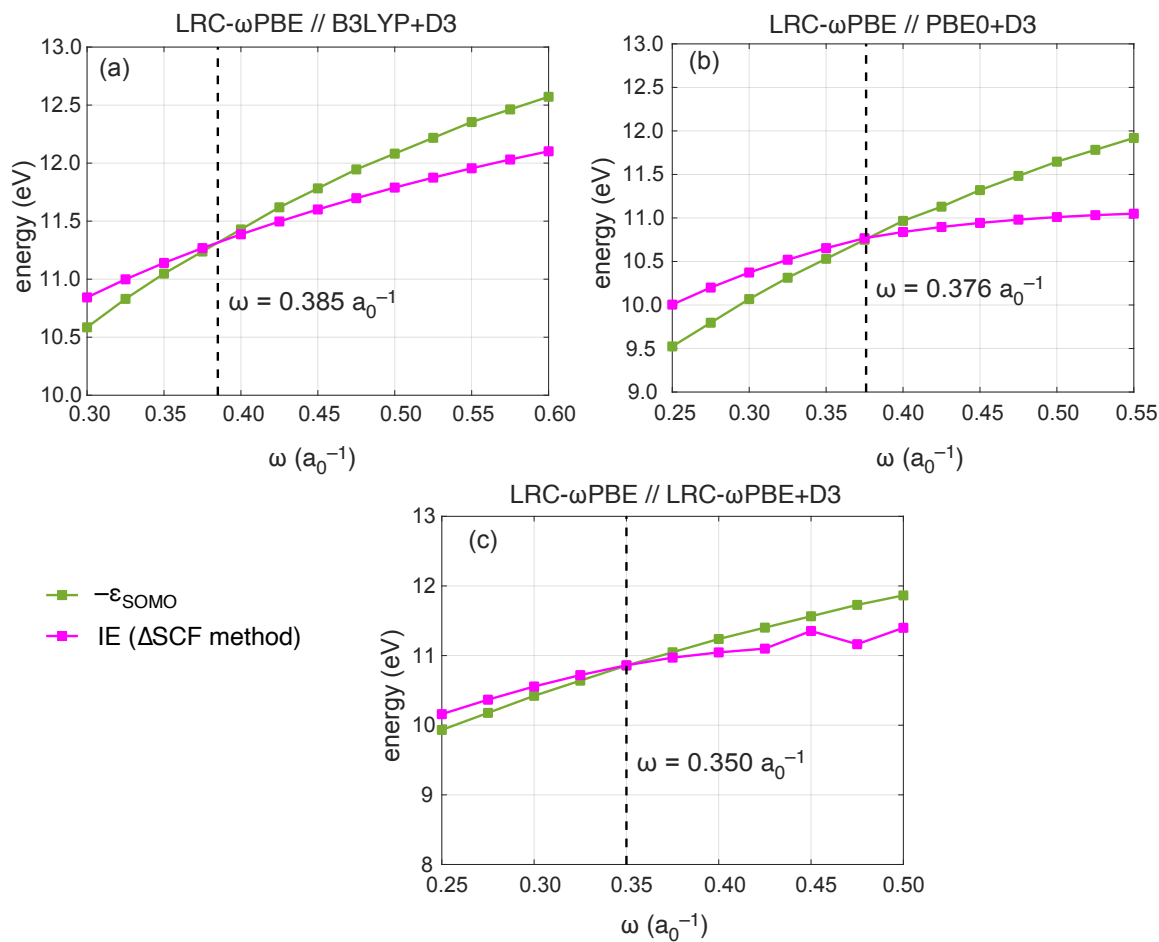


Figure S20: Optimal-tuning plots, obtained using the LRC- ω PBE functional, for representative snapshots from QM/MM simulations using (a) B3LYP+D3, (b) PBE0+D3, and (c) LRC- ω PBE+D3.

7 Absorption Spectra

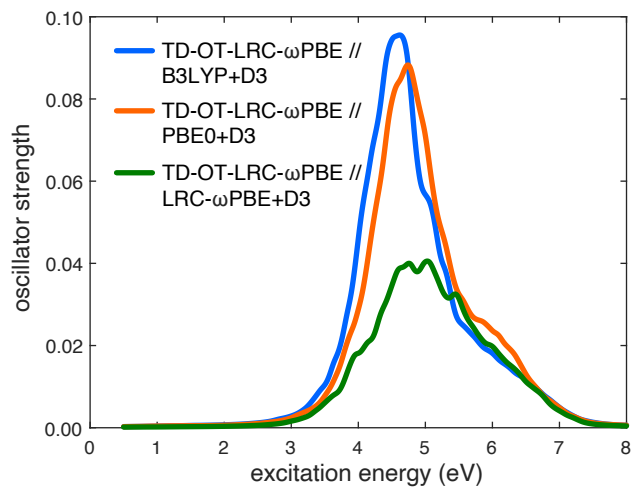


Figure S21: Ensemble-averaged distributions of oscillator strength (without any normalization), computed using TD-DFT with the OT-LRC- ω PBE functional applied to snapshots obtained from three different QM/MM trajectories, as indicated.

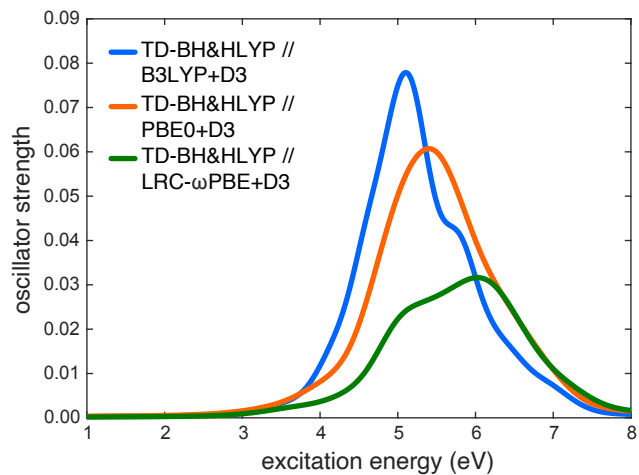


Figure S22: Ensemble-averaged distributions of oscillator strength (without any normalization), computed using TD-DFT with the BH&HLYP functional applied to snapshots obtained from three different QM/MM trajectories, as indicated.

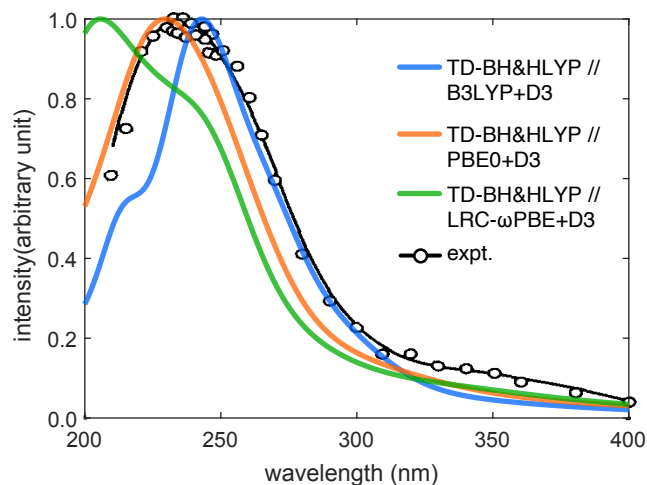


Figure S23: Comparison of the ensemble-averaged absorption spectra obtained using TD-BH&HLYP calculations with liquid configurations taken three different QM/MM trajectories as indicated. The results are overlaid with the experimental spectrum from Ref. 1. Intensities have been scaled so that the maximum of each individual spectrum is unity, but the spectra are not otherwise adjusted.

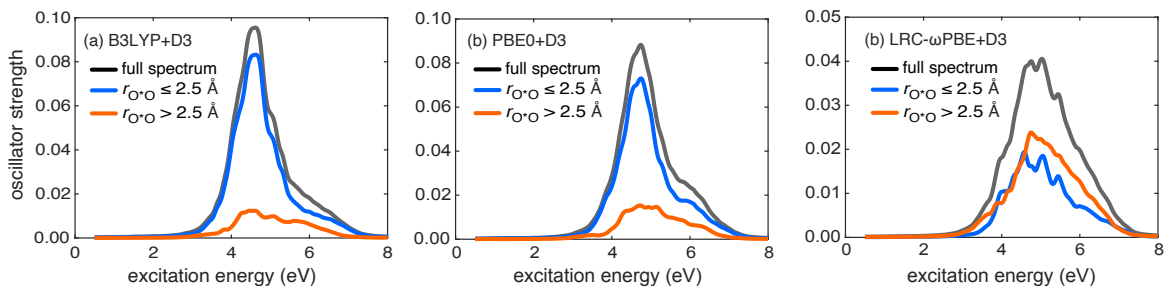


Figure S24: Decomposition of the ensemble-averaged TD-DFT absorption spectrum according to the value of r_{O^*O} , for QM/MM trajectories using (a) B3LYP+D3, (b) PBE0+D3, and (c) LRC- ω PBE+D3. The TD-DFT calculations were performed using the OT-LRC- ω PBE functional in each case.

References

- [1] G. Czapski and B. H. J. Bielski, Absorption spectra of the $\bullet\text{OH}$ and $\text{O}\bullet^-$ radicals in aqueous solutions, *Radiat. Phys. Chem.*, 1993, **41**, 503–505.